

Simulations of Laser-Driven Magnetized-Liner Inertial Fusion

Leah H. Xiao

Webster Schroeder High School

Advisor: **Dr. R. S. Craxton**

Laboratory for Laser Energetics

University of Rochester

November 2016

1. Abstract

Magnetized Liner Inertial Fusion (MagLIF) is being explored as a new method of producing fusion. MagLIF uses a cylindrical metal shell, or liner, containing deuterium fuel. A high electric current is run through the liner, forming a strong magnetic field and causing implosion of the cylinder. A preheating beam is fired down the axis of the cylinder to heat the deuterium so that when the liner implodes and the deuterium is compressed, the deuterium is able to reach the high temperatures needed for fusion. In this exploratory research work, simulations using the hydrodynamics code SAGE were conducted to help understand the physics of MagLIF. Simulations of MagLIF experiments on the OMEGA laser system at the University of Rochester Laboratory for Laser Energetics (LLE) without the preheating beam have demonstrated agreement with data from experimental shots. By varying the parameters of the beams used to implode the cylinder, the simulations have found the optimum conditions for achieving a uniform implosion with the OMEGA system. Simulations of upcoming shots on the OMEGA system with the incorporation of the preheating beam predicted temperature profiles of the heated deuterium-filled cylinder. SAGE was also used to simulate large-scale targets with dimensions similar to those of the Z-machine at Sandia National Laboratory. The simulated temperature profiles due to preheating are consistent with the experimental observations in four shots, a control shot and three variations. Simulations of the Z-machine with a higher deuterium density, as desired for future experiments, show that the proper temperature profile is achieved through the formation of a self-focusing density channel.

2. Introduction

Inertial confinement fusion (ICF) is a process that utilizes high powered lasers, X rays, ion beams or other energy means to compress and implode a target made up of a plastic or metal shell filled with deuterium-tritium fuel. The shell of the target ablates outward, compressing the contents inside the shell to reach temperatures of several keV (1 keV = 11.6 million degrees K). At the very high temperature and pressure, the nuclei can overcome the Coulomb force between them to achieve nuclear fusion. Most ICF research is done using lasers to implode the target.¹ Recently, an alternative method known as Magnetized Liner Inertial Fusion (MagLIF)² is being explored.

As illustrated in Figure 1, MagLIF utilizes a cylindrical target surrounded by a shell or liner that contains deuterium, which is heated with a laser beam called the “preheating beam” fired perpendicular to one circular end of the cylinder or “window” before implosion occurs. There are two different systems on which MagLIF experiments are currently run. The first is Sandia National Laboratory’s Z pulse power machine, and the second is the OMEGA laser system at LLE.

Sandia’s Z-machine uses an electric current pulse running through the liner to generate a strong magnetic field to implode the liner (Figure 1b). A second current is run through a set of external coils (Figure 1a) generating another magnetic field that becomes compressed when the deuterium compresses, which keeps the α -particles released from the fusion contained within the cylinder. This containment contributes to the heating of deuterium to fusion temperature. The preheating beam (red arrow) is an essential part of MagLIF^{2,3} because it heats the deuterium before implosion begins, allowing the deuterium to reach higher temperatures when compressed, increasing the number of fusion reactions. Additionally, the temperature needs to be high enough to maintain the current and the magnetic field. If the temperature drops too low, the current and thus the magnetic field dissipate.

Because the facilities needed to run the required current through the liner are large and expensive and there are a limited number of experimental shots that can be conducted (approximately one per day), small-scale MagLIF experiments are being carried out using

OMEGA, with the liner imploded by laser beam irradiation with beams known as “drive beams” instead of the electric current and magnetic field, as seen in Figure 1c.

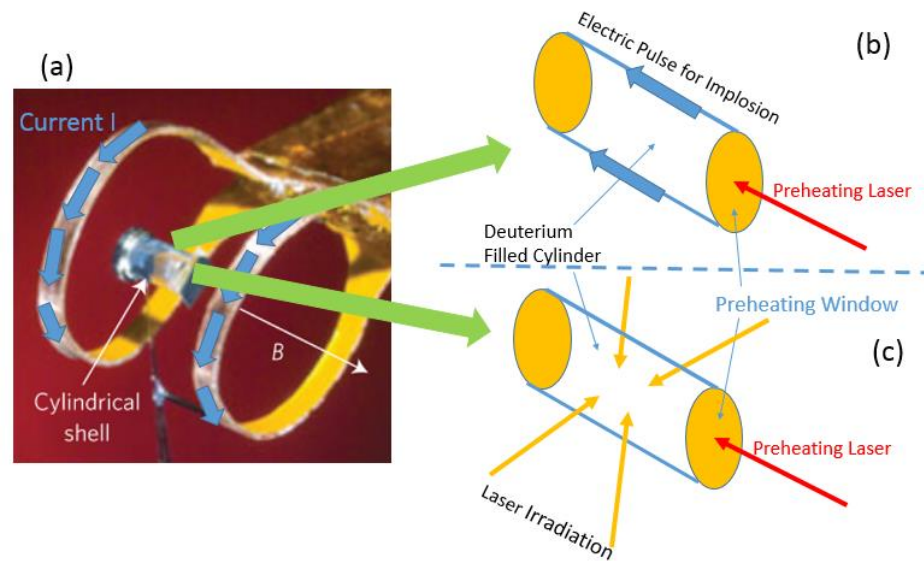


Figure 1: (a) Configuration of the MagLIF set up, showing a cylindrical liner (shell) filled with deuterium and coils that generate a magnetic field B along the axis of the cylinder when current is passed through. (b) Diagram of MagLIF with magnetic compression. The current is illustrated by the blue arrows, while the preheat beam is shown in red. (c) Diagram of the laser implosion configuration of MagLIF with the yellow arrows representing laser drive beams. The face of the cylinder where the preheat beam enters features a thinner wall called the window.

In this exploratory work, the hydrodynamics code SAGE⁴ was used to understand aspects of the physics of MagLIF preheating and compression. This research demonstrates that SAGE is suitable to simulate these aspects of MagLIF. Proving this allows SAGE to be used to guide the designs for future MagLIF experiments.

3. MagLIF Experiments on the OMEGA System

Small-scale MagLIF experiments with laser beams irradiating the liner are being carried out using the OMEGA laser system. A detailed cross section of the liner and a 2D view of the upper half of the liner (which is rotationally symmetric about the z -axis) are shown in Figure 2.

The liner wall is made of CH (carbon-hydrogen, plastic). The thickness of the liner wall is $20\ \mu\text{m}$. The preheating window, which is approximately $2\ \mu\text{m}$ thick, contains the high-pressure deuterium. There are four beams in Figure 2. Beam 1 and Beam 4 are symmetric about the middle plane of the cylinder, as are Beams 2 and 3. Each of the implosion beams illustrated actually represents ten beams that encircle the outside of the cylinder. MagLIF implosions on OMEGA use 40 beams.

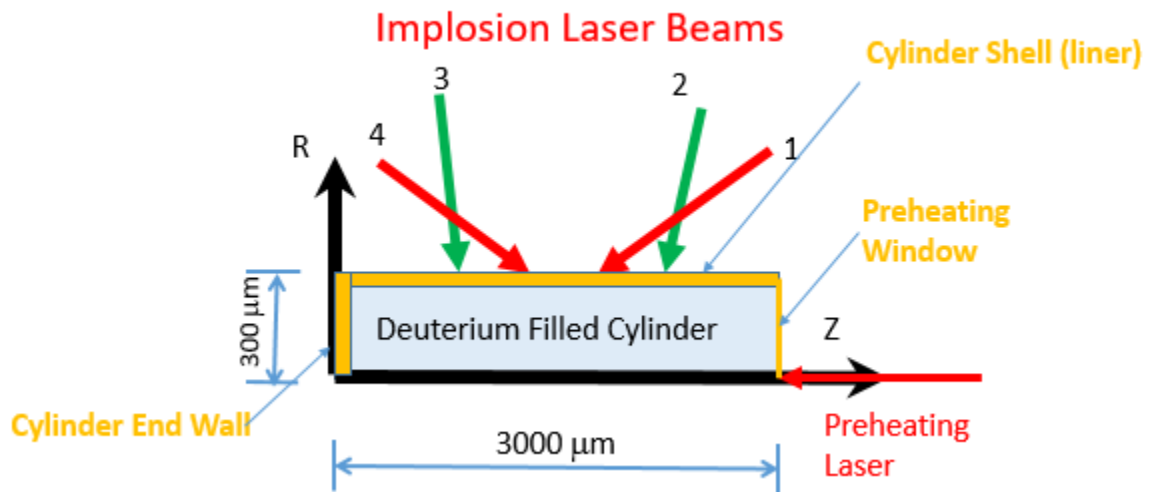


Figure 2: Cross Section of the MagLIF target used in the OMEGA system.

Simulations were conducted without the preheating beam to examine the speed and uniformity of compression (Section 3.1) and with the preheating beam to predict the results of future experiments (Section 3.2).

3.1 Experiments without Preheating

A series of experimental shots were conducted, without the preheating beam, to study compression. A simulation of one of these shots is shown in Figure 3, which illustrates implosion indicated by the shell surface collapsing inwards at $1.4\ \text{ns}$ after irradiation starts. What is shown is the upper half of the cross section of the cylinder with only two groups of laser beams (Beam 1 and Beam 2 from Figure 2) pictured on one side of the cylinder for clarity. Density contours are shown in dark blue. The critical density, or the highest density that the beams can penetrate is shown in orange. When laser rays encounter areas of higher density, they refract away. The laser

wavelength is $\lambda = 0.351 \mu\text{m}$, the third harmonic of the Nd: glass laser whose wavelength is $1.054 \mu\text{m}$.

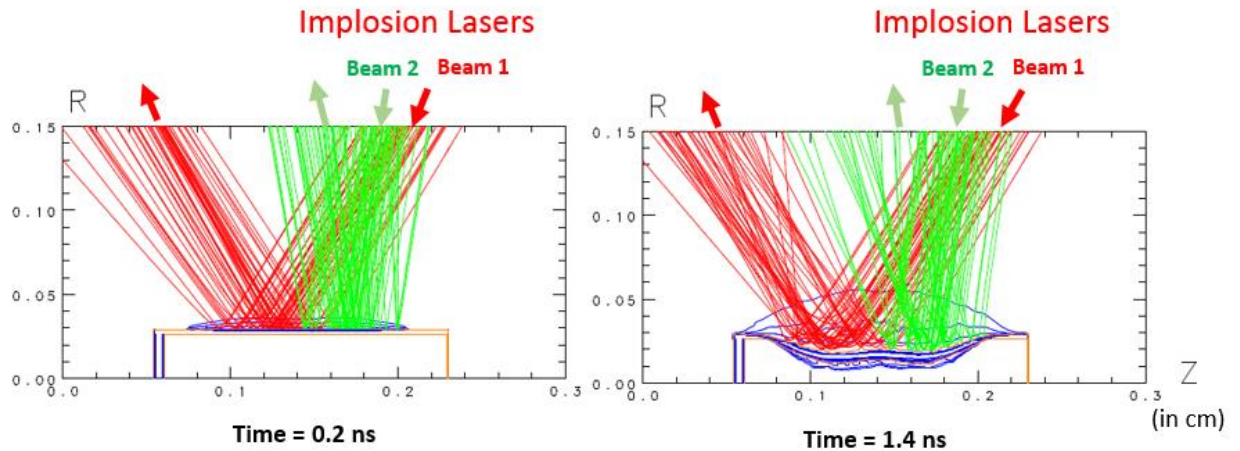


Figure 3: Two simulation snapshots showing two implosion beams (green and red) irradiating the liner and imploding the CH wall from experimental shot 79495. All units on such plots are in centimeters.

Figure 4 shows x-ray emission images from $t = 1.6 \text{ ns}$ to $t = 1.8 \text{ ns}$. These images illustrate the speed of implosion, the portion of the cylinder that is compressed and the uniformity of the implosion. In Figure 4, the darker areas are from stronger emissions. The compression is fairly uniform, indicated by the smooth central region in each of the images. The x-ray emission comes from the hot plasma outside of the shell heated by the laser (Figure 3) and was used to determine the shell's location from experimental shot 79495. This was found by locating where the x-ray emission drops off sharply on the inside of the darker areas. In the top row of images in Figure 5, these radii were plotted for each z , creating an outline of the shell. The experimental images do not explicitly indicate a center of each cylinder, so the coordinates of the center of the cylinder needed to be found. This was done by trial and error to properly place the cylindrical edges, adjusting the coordinates of the center until the closest alignment between the red and blue dots was found.

The graphs of these points were compared with graphs of simulated shell center of mass plotted from SAGE calculations. The center of mass is the location that represents the mean position of mass in a system. D. Barnak⁵ conducted a simulation of the x-ray emission based on a SAGE calculation that found that the x-ray emission is about $47 \mu\text{m}$ offset above the simulated

center of mass, resulting in the offset between the dots (experimental results) and the black line (simulated center of mass) in the first row of images. When the predicted offset is eliminated, as shown in the second row of graphs, the dots from the experimental shot and the black line from the simulation align very well. The width of the flat compression of the x-ray emission is about the same as the width of flat compression of the simulated center of mass plot, which is about $600\ \mu\text{m}$.



Figure 4: *X-ray emission images⁶ of implosion from experimental shot 79495 from 1.6 to 1.8 ns.*

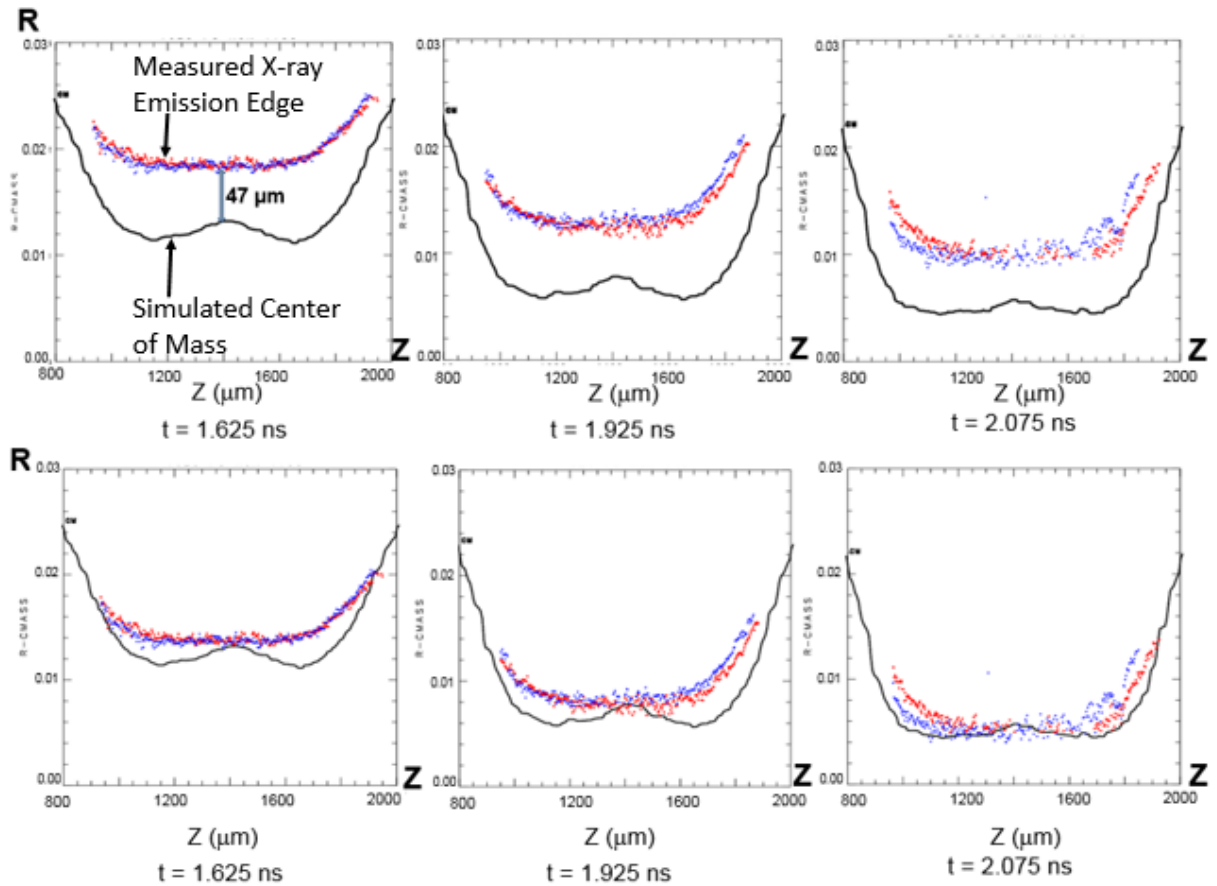


Figure 5: Top Row: Measured x-ray emission edge radius as a function of Z obtained from images such as those in Figure 4, plotted with SAGE predictions of center of mass. The red and blue dots show the x-ray emission from the opposite sides of the shell. Bottom Row: The x-ray radii have been reduced by $47\ \mu\text{m}$ to remove the predicted offset. In these images, the z-axis ranges from 0.08 cm to 0.2 cm and the r-axis ranges from 0.0 cm to 0.03 cm.

To compare the rate of compression, the experimental x-ray emission radii (from 8 images like those in Figure 4) and the simulated center of mass radii were plotted over time in Figure 6. The slope of each represents the rate of compression. The plots have very similar slopes, indicating similar implosion speeds. (The experimental implosion speed is 2.1×10^7 cm/s and the simulated implosion speed is 1.7×10^7 cm/s). Exact agreement is not expected as the separation between the x-ray emission radius and the center of mass radius changes over time. The results demonstrate that the velocity obtained from the x-ray emission radius gives a good indication of shell implosion velocity.

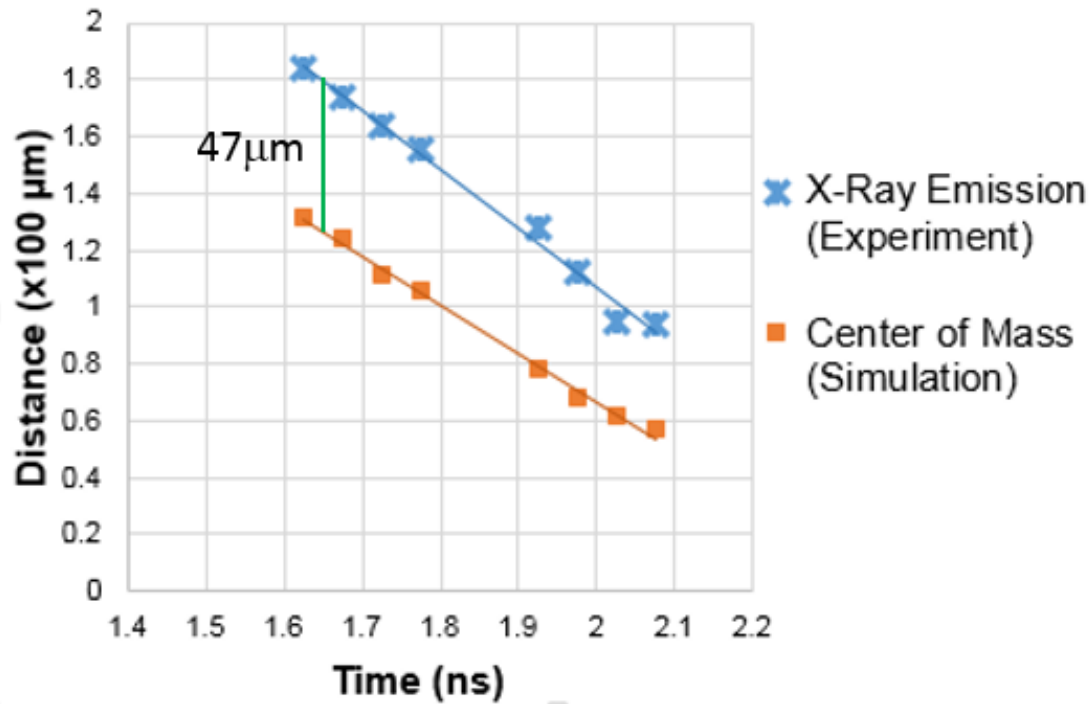


Figure 6: Experimental X-ray emission radii and simulated center of mass radii as a function of time, obtained from eight images such as those shown in Figure 4. The straight lines are regression fits.

A series of SAGE simulations was run to improve the liner shell implosion uniformity along the Z-direction. By shifting the beam pointings of beams 1 and 4 towards the outer sides of the cylinder in the z direction and shifting the beam pointings of beams 2 and 3 towards the center of the cylinder in the z direction and adjusting beam energy levels, significant improvements were made, as shown in Figure 7. The image on the left depicts the liner center of mass as a function of Z for one of the earlier runs. The liner's center of mass plot for times from 0.6 ns to 1.2 ns shows that the implosion is not uniform across the Z-direction. The graph on the right shows a more uniform compressed section during the implosion after optimization.

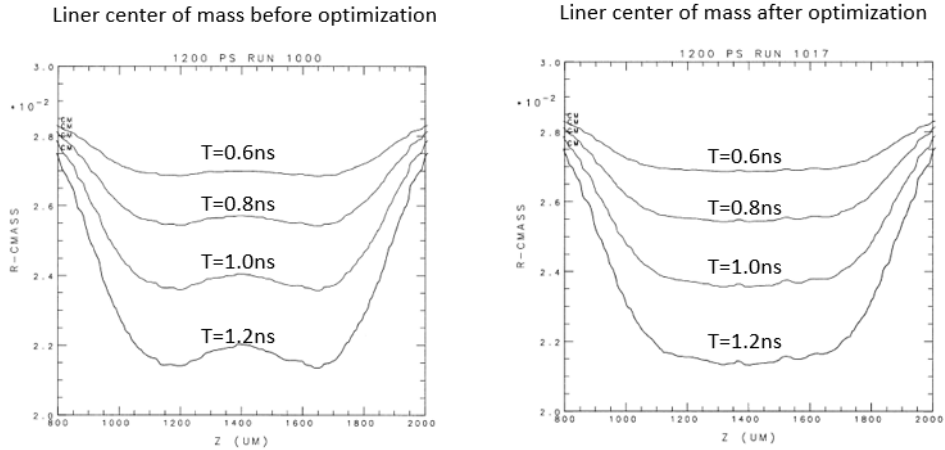


Figure 7: Center of mass radius as a function of z for 4 successive times, before and after optimization of the laser beam pointings. The z -axis ranges from .08 cm to 0.2 cm and the r -axis ranges from 0.02 cm to 0.03 cm.

3.2 Experimental Shots with Preheating

Results from planned laser driven MagLIF shots on OMEGA including the preheat beam were predicted using SAGE. A simulation at $t = 1.4$ ns is shown in Figure 8. Implosion has not yet begun because the drive beams have just been initiated after the preheat beam has been firing for 1 ns. The planned set-up is comprised of a long tube that contains the deuterium, so in the simulation, the left end of the cylinder has been eliminated to reduce extraneous factors. The right end of the cylinder has been extended as well. The dark blue density contours on the right end arise from plasma created by the penetration and heating of the window. The density of the D_2 changes as it is heated, causing some laser rays to refract toward the axis and some to refract towards the shell. The issue with the preheating beam hitting the shell, as demonstrated by Figure 8, is that when the shell is heated by the preheating beam, it creates plasma that expands inwards and mixes with the deuterium. Radiation loss scales as Z^2 , or the square of the number of protons in the nucleus. Because the carbon radiates about thirty-six times more than the deuterium (beryllium, which is the preferred shell material for current-driven implosion, radiates about sixteen times more than deuterium), the temperature of the compressed fuel decreases because of the radiation energy losses, resulting in less fusion energy.

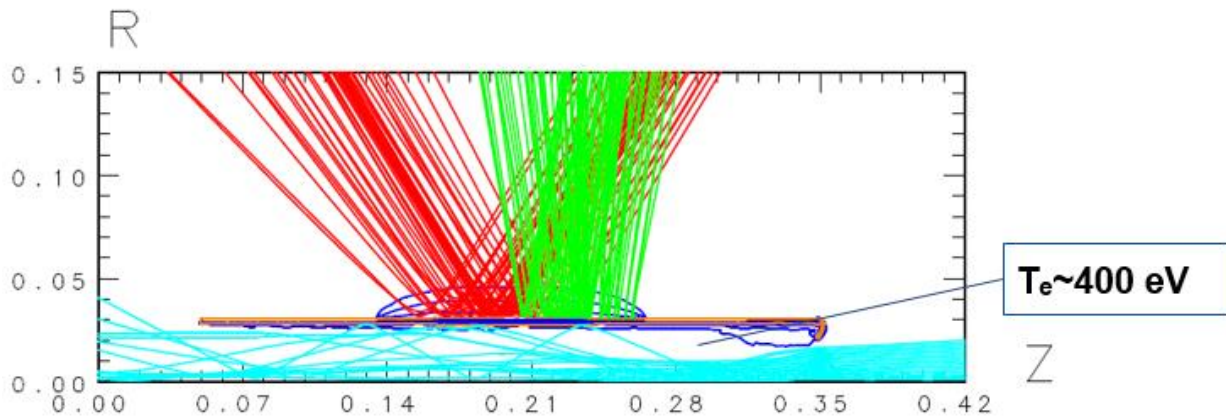


Figure 8: Simulation of a planned experiment on OMEGA at $t= 1.4$ ns. In addition to the beams that drive the implosion (red and green), the preheating beam (teal) enters from the right.

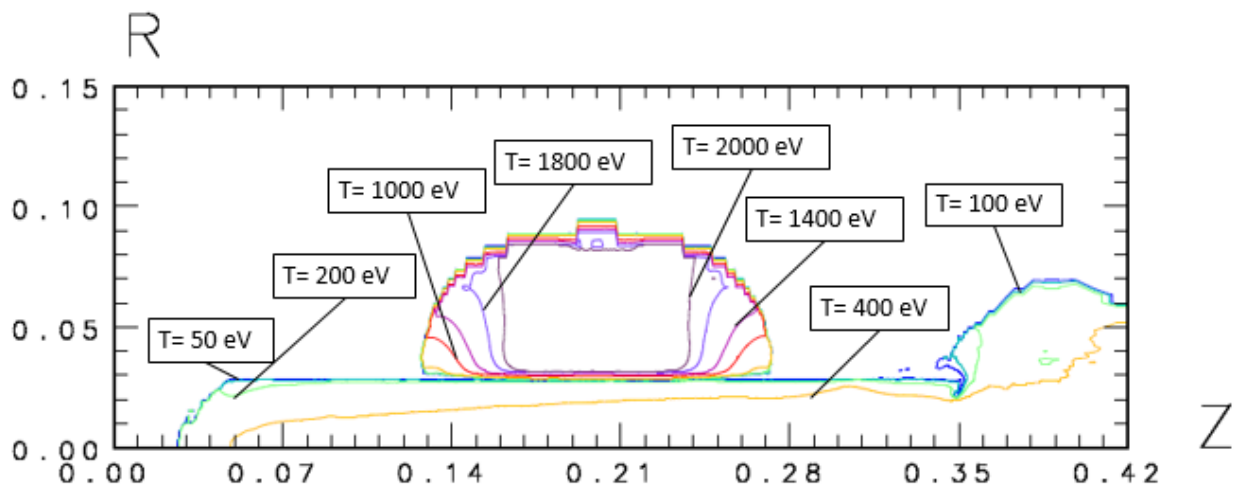


Figure 9: Temperature contours of an OMEGA simulation at the same time as Figure 8. The blue contour is 50 eV, the teal is 100 eV, the green is 200 eV, the yellow is 400 eV, the red is 1000 eV, the light purple is 1400 eV, the indigo is 1800 eV and the dark purple is 2000 eV.

Figure 9 shows temperature contours at the same time as Figure 8. The central region of the image has been heated by drive beams, which is why the temperature reaches around 2000 eV. In the deuterium, the hottest region is around the axis, which reaches around 400 eV. The temperature is above 200 eV for all of the deuterium in the cylinder, extending all the way up to

the shell. The temperature should be at least 100 eV by the time the cylinder starts compressing. This simulation shows that the preheating is sufficient, but could potentially cause plasma mixing due to rays striking the inner wall of the shell.

4. Simulations for Large-scale Systems

SAGE has also been used to simulate large-scale targets with dimensions similar to those of the Z-machine at Sandia National Laboratory. The Z-machine uses a cylindrical target approximately ten times the length and radius of the OMEGA target (the length changes from 0.1750 cm (Figure 3) to 1.2 cm, the radius changes from 300 μm to 2600 μm and the thickness of the shell changes from 30 μm to 300 μm). In the Sandia Z-machine experiments the shell is imploded with a strong current pulse run through the metal liner in the z-direction. This current produces a magnetic field. Since SAGE does not have the capability of modeling the current and magnetic field driven implosion, laser beams are used to simulate the implosions caused by the electric current. Simulations were conducted to examine aspects of preheating on Z-machine experiments (Section 4.1) and predict the results of future large-scale experiments (Section 4.2)

4.1 Experiments on Sandia's Z-machine

A series of experimental shots were done on the Z-machine using a preheat beam with a second harmonic wavelength ($\lambda= 0.527 \mu\text{m}$, see Section 3.1) The beam diameter is determined by different phase plates, sheets of glass similar to frosted glass that focus the beam to specific radii. The preheat beam lasts for 2.0 ns. The effects of preheat beam energy, beam diameter and deuterium density were tested. The results are shown in Figure 10.

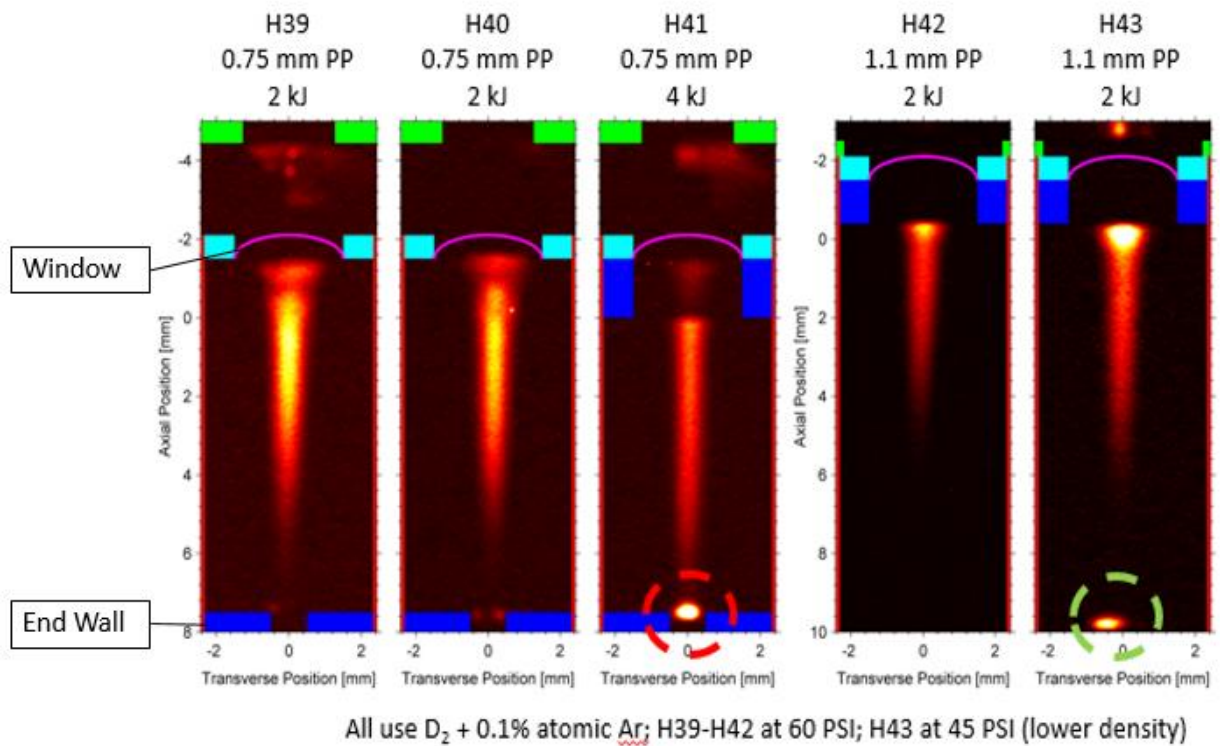


Figure 10: Time integrated images from experiments on the Z-machine showing x rays released from the heated deuterium, which are produced by a trace amount of argon in the deuterium. The yellow to red to black color scale shows the temperature change from high to low. H39 and H40 are the control shots and are nominally identical.

Time-integrated x-ray images⁷ from these experiments are shown in Figure 10. In shots H39 and H40, the preheating laser energy is 2 kJ and the beam diameter is 0.75 mm. H41 has the same setting except that the preheating laser energy is doubled to 4 kJ. In H42, the diameter of the beam is increased from 0.75 mm to 1.1 mm, decreasing the intensity of the preheating laser. H43 is similar to that of H42, except that the density of the deuterium is lower. In two shots (H41 and H43), the preheating beam penetrates the deuterium more easily to reach the cylinder's end wall as indicated by the bright spot inside the red and green circles.

Figure 11 shows temperature contours from a simulation of shot H39. Temperature contours in areas beyond the shell (the shell location is indicated by yellow on the first temperature contour plot at $t=0.5$ ns) are caused by drive laser heating and should be ignored when discussing the effect of the preheat beam. For this particular set of experimental shots,

implosion was not initiated. The incorporation of the drive beams in the simulation did not impact the results because the shell had barely begun to move at the time the preheat beam was firing. Following the end of the preheat beam firing, the temperature of the deuterium begins to cool off, as in the temperature contours at $t=3.0$ ns. The narrow channel that is heated stays well away from the liner at all of the times in Figure 11, and temperatures in the channel generally range from 400 eV to 1000 eV when the preheat beam is on. The temperature profiles near the cylindrical axis in the simulation agree very well with the x-ray emission image. In Figure 11, where there are higher temperatures in the simulated temperature contours there are higher temperatures indicated by the x-ray images (indicated by the lighter colors, such as yellow, in the x-ray image on the lower right corner).

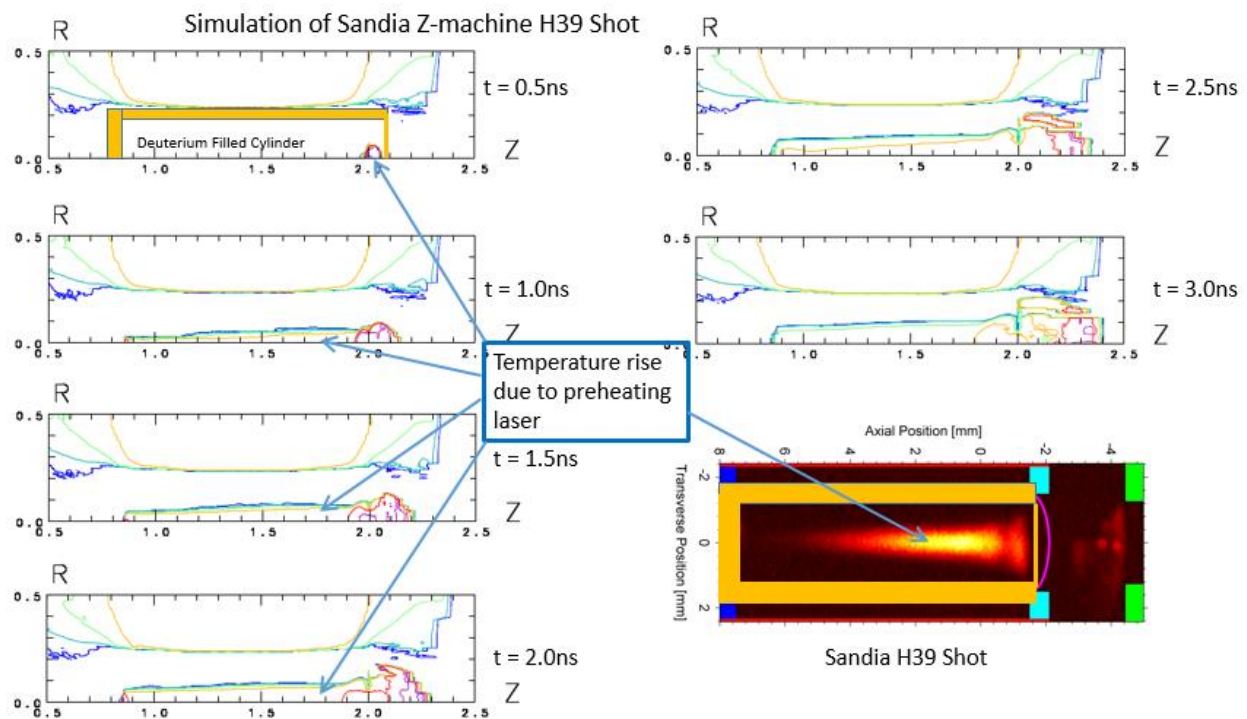


Figure 11: Temperature contour plots from a simulation of the Sandia Z-machine H39 shot illustrating the temperature changes at times measured from when the 2-ns preheating beam is turned on ($t=0$ ns). The lower right figure is the time-integrated experimental x-ray emission image, which corresponds to a combination of the simulations during the preheating laser firing. Yellow boundaries have been added to show the locations of the cylinder walls. As in Figure 9, in the simulated temperature contours, the blue contour is 50 eV, the teal is 100 eV, the green is 200 eV, the yellow is 400 eV, the red is 1000 eV and the purple is 1400 eV.

Figure 12 shows a direct comparison between both the simulated temperature contours and the x-ray emission images of the control shot (shot H39) and the shot with twice the beam energy (shot H41). The higher laser power enables the beam to penetrate the entire length of the cylinder and hit the cylinder's end wall opposite the window. This creates a hot zone near the wall which can clearly be seen in the H41 simulation results in the red circle on the lower left and the experimental shot image in the red circle on the lower right. Some rays reflect off the end wall, heating the deuterium in that area twice, further contributing to the creation of the hot spot.

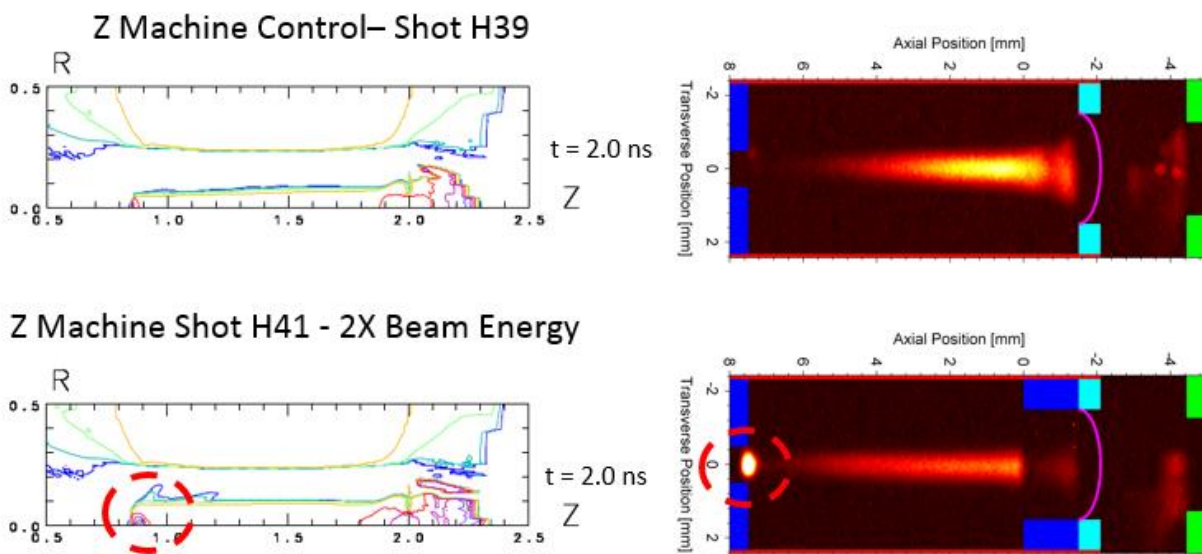


Figure 12: A comparison between Shot H41 with the control shot, Shot H39 at $t = 2.0$ ns. In Shot H41, the preheating laser energy is doubled from 2 kJ to 4 kJ.

In Figure 13, the control (shot H39) is compared with a shot (H42) with a larger beam diameter. Because the beam is more widely distributed in the radial direction, the intensity of the beam lowers, which results in a narrower heated region, seen in both simulated and experimental results. There is actually a greater amount of heated area, but most of this area is below the lowest contour (50 eV), so it does not display.

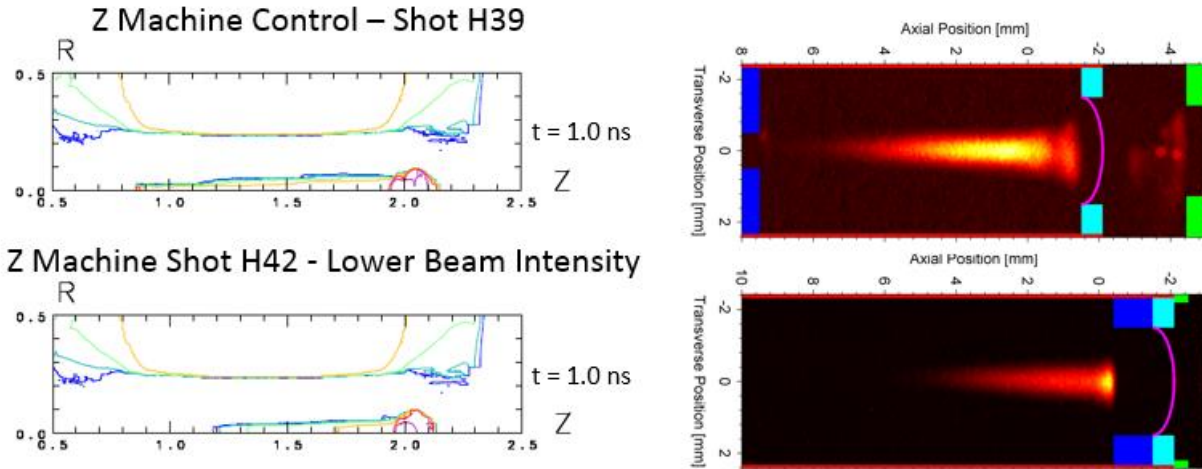


Figure 13: Comparison between Shot H42 and the control shot, Shot H39 at $t=1.0$ ns, midway in the preheating pulse. In Shot H42, the phase plate diameter is increased from 0.75 mm to 1.1 mm, reducing the preheating laser energy intensity.

From both the simulation and the experimental image, it can be inferred that the preheating beam in shot H42 does not penetrate as far into the deuterium, nor does it heat as wide of a range in the radial direction. In the simulation, the yellow temperature contour for 400 eV ends midway through the deuterium rather than occupying the whole length of the cylinder, while in the experimental image, the hot x-ray emitting region ends abruptly at around the same location that the simulation's strong heating ends.

Figure 14 compares two shots that both use the lower-intensity larger beam. Shot H42 is the control for this comparison. The other is shot H43, which lowers the density of the deuterium from 60 psi (0.664 mg/cm^3) to 45 psi (0.5 mg/cm^3). It can be seen from the simulation temperature profiles and the experimental images that the beam is penetrating more in the lower density setting, approximately 1 mm to 2 mm in each case. This is because the lower density deuterium does not absorb heat as well.

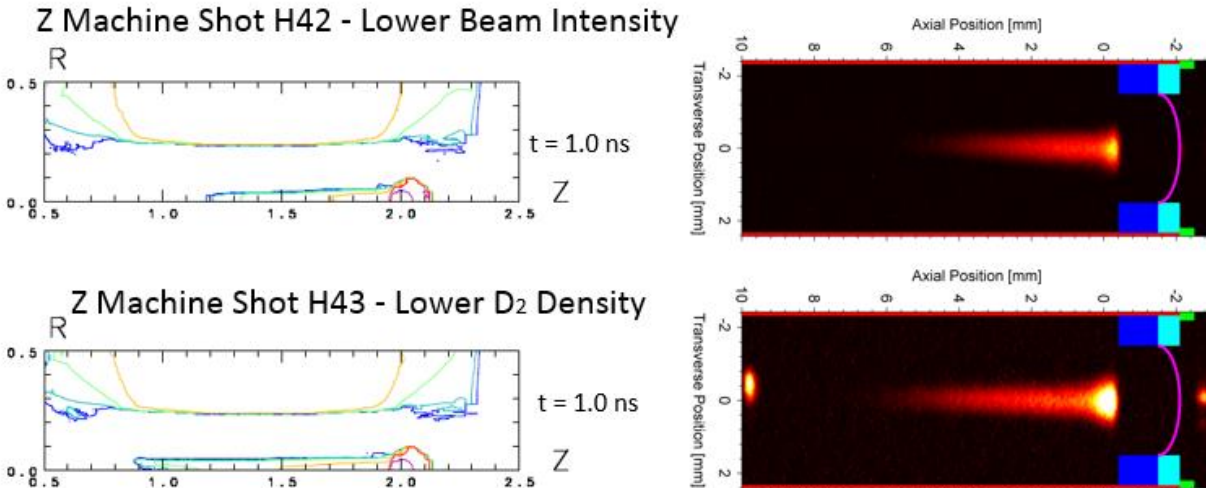


Figure 14: A comparison between Shot H43 and Shot H42. In Shot H43, the deuterium density is reduced compared to Shot H42 (from 0.664 mg/cm^3 to 0.5 mg/cm^3).

Through this series of comparisons, the validity of SAGE simulations is further demonstrated on the Sandia Z-machine.

4.2 Future Large-scale Systems

SAGE was used to simulate future Z-scale experiments, with the desired higher density of 3 mg/cm^3 and a 2-ns third-harmonic preheating beam. Figure 15 illustrates such a simulation. There are only two drive beams used for implosion. For clarity, only one drive beam is shown (red). Only one ray of the preheating beam is shown (teal) to more easily view the behavior of the system while preheating is occurring. The energy of the preheat beam was given as 2 kJ. The preheat beam turns on 20 ns after the drive beams have begun firing (just after the shell has started to move). Multiple trials were run, testing different energies and positions of the drive beams along the z-axis to ensure that the shell imploded uniformly at around 80 ns, which is expected for a magnetically driven implosion. The drive beams were aimed at about the center of the cylinder in the z-direction. The total energy of both beams is 1.4 MJ (700 kJ for each drive beam).

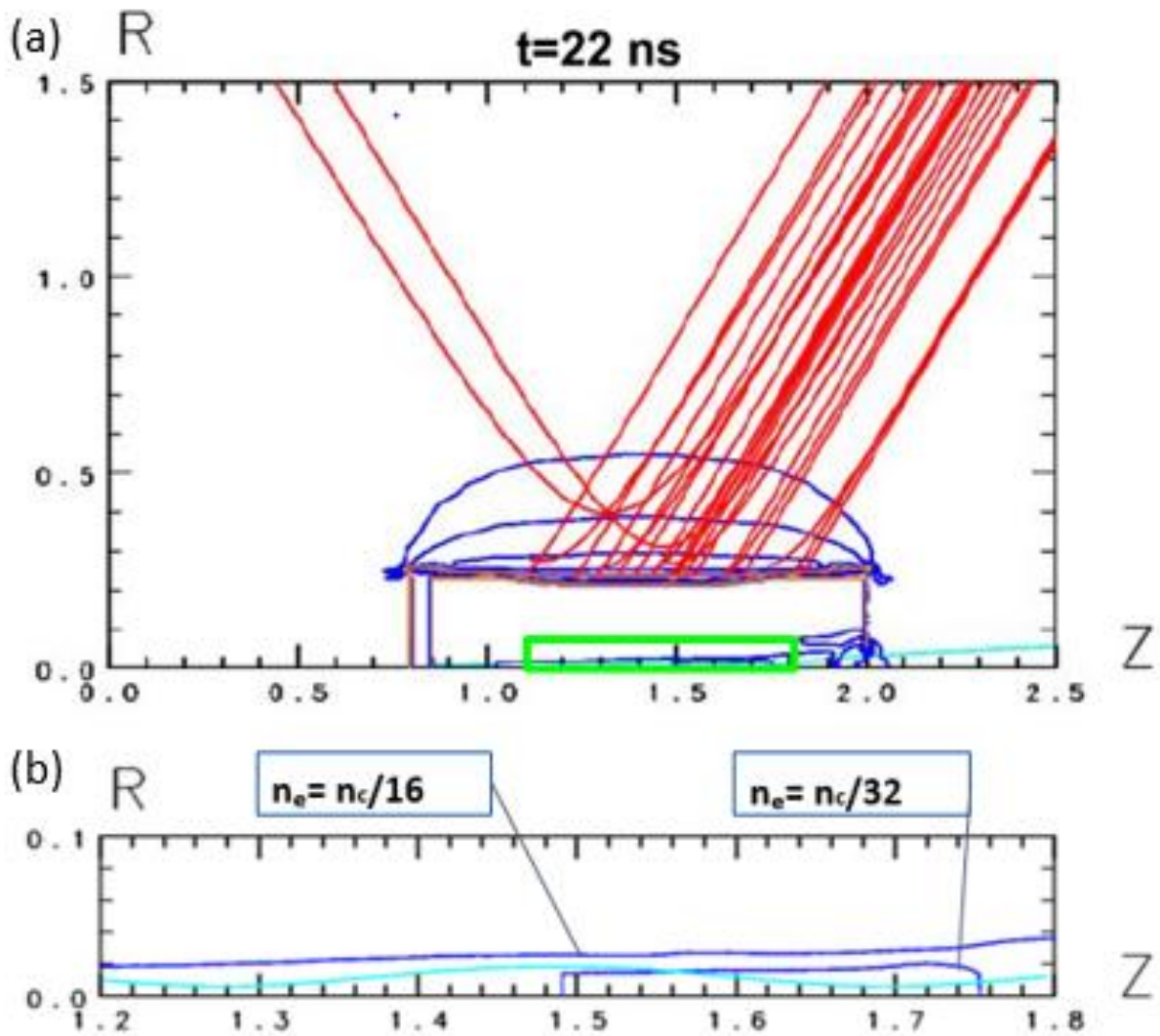


Figure 15: Example simulation of a future experiment with a higher density deuterium gas. Image 15a shows the liner being imploded by a laser beam with density contours in blue. Image 15b is an expansion of the area in the green box showing that the contour farther from the axis has a higher density than the contour closer to the axis, indicating the formation of a low-density channel. N_c represents the critical density. A sample laser ray (teal) is confined to the channel by refracting away from the higher-density contour.

Here, in contrast to the OMEGA simulation of Figure 8, it can be clearly seen that the preheating beam stays in a narrow channel along the axis of the cylinder, which avoids the preheat beam hitting the inside of the shell. When the deuterium near the axis is heated, it expands outwards toward the upper region. This leaves the region near the axis with a lower density. Figure 15b shows a typical ray of the preheating beam indicated in teal. When this ray refracts outwards, it encounters the higher density deuterium, which refracts it back towards the axis, keeping the beam focused near the axis of the cylinder. This is called whole-beam self-focusing.⁴ The channel becomes more pronounced as time increases. The importance of the channel is that it allows the region of the cylinder near to axis to be heated effectively and uniformly without disturbing the shell.

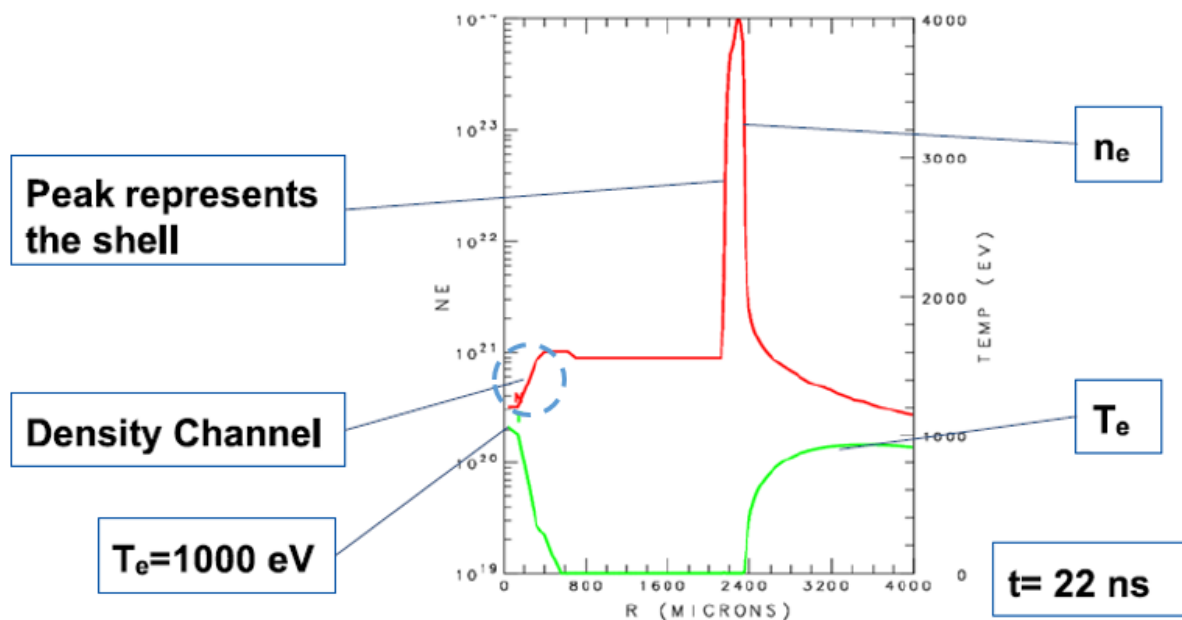


Figure 16: A one-dimensional graph in the radial direction at the midpoint along the z-axis of the cylinder. The red line represents density (in units of electrons/cm³) and the green line represents the temperature. The region in the blue circle illustrates the density channel.

Figure 16 helps to illustrate the density channel by plotting density (red) and temperature (green) in the radial direction at the midpoint of the cylindrical target. The density channel location is circled in blue. The density has a clear dip towards the center of the target when r is less than $400 \mu\text{m}$. This is consistent with the idea that the deuterium expands outwards, leaving the center of the cylinder less dense. Moving along the r -axis, the density rises and peaks at a

density higher than the initial density from about $r=400\ \mu\text{m}$ to $700\ \mu\text{m}$. This is because the deuterium from the expansion is pushed outwards. From the temperature graph (green), it is clear that the temperature peaks on the axis, which is consistent with the theory that all the laser energy is deposited in the density channel containing the beam.

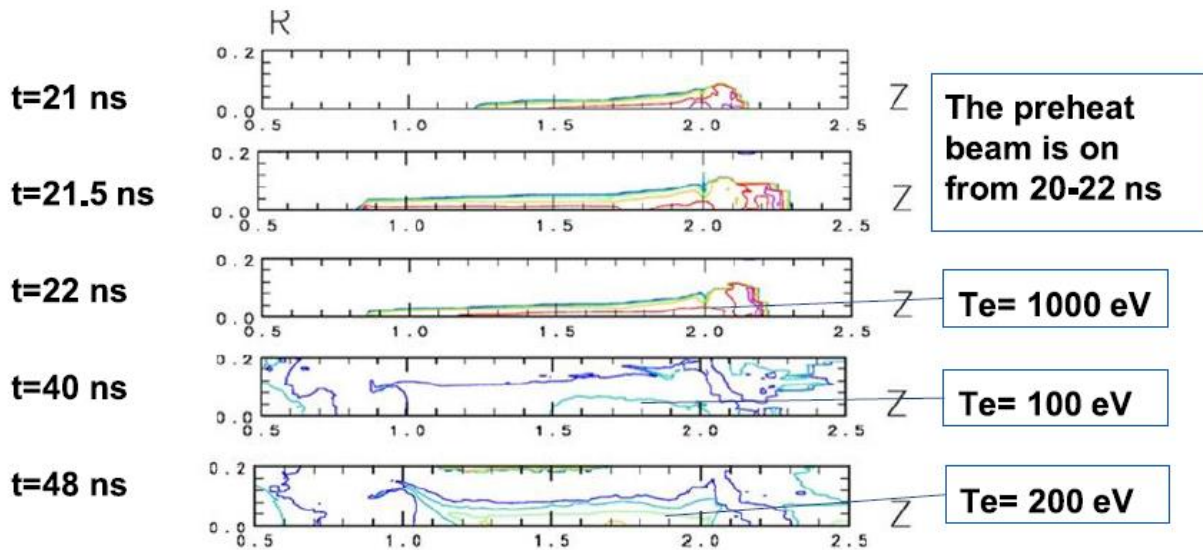


Figure 17: Temperature contours showing the temperature progression in the cylinder over time. The preheating beam was on from $t = 20\ \text{ns}$ to $22\ \text{ns}$.

Figure 17 shows the progression of temperature of the deuterium contained in the cylinder over time. The first three strips ($t=21\ \text{ns}$ to $22\ \text{ns}$) show the temperature contours while the preheating beam is on. The deuterium is heated quickly along the axis to high temperatures of $1000\ \text{eV}$, all while being extremely well confined to the core of the cylinder. After the preheating beam switches off, the deuterium near the axis cools and the surrounding deuterium becomes hotter by thermal conduction, which is desired. This temperature change is indicated by the temperature contours at the 40-ns plot. However, once the deuterium begins to be compressed due to the implosion of the liner, the temperature of the deuterium increases again to about $200\ \text{eV}$ at $48\ \text{ns}$.

This preheating beam self-focusing and the effective heating of the center of the cylinder to an ideal temperature evenly along the axis without disturbing the shell is significant because it confirms the effectiveness of the preheating beam in the MagLIF approach and helps clarify the physics of the preheating mechanism.

5. Conclusion

This work showed that SAGE is an effective tool to model both OMEGA and Sandia Z-machine MagLIF experiments. A variety of MagLIF experiments have been modeled with different geometries and beam characteristics. Simulations of OMEGA experiments without a preheat beam demonstrate agreement with experimental observations. Simulations of upcoming OMEGA shots with the preheat beam predict temperatures of ~ 400 eV. Simulations of Z-machine preheating show agreement with observations from experimental shots. Simulations of the Z-machine with a higher deuterium density, as desired for future experiments, show that the desired temperature profile is achieved through the formation of a self-focusing density channel. This is, to our knowledge, the first time that self-focusing has been reported in MagLIF physics.

6. Acknowledgments

This project was made possible by Dr. Craxton, whose support and assistance has guided me through this process. He has truly been an incomparable adviser. I would like to thank Mr. Barnak and Dr. Davies for providing the experimental data and images. I also would like to thank Dr. Enck for inspiring me to pursue physics outside of the classroom and encouraging me to apply for this internship. Lastly, I would like to thank the Laboratory for Laser Energetics for this incredible program that has been a wonderful learning experience.

7. References

-
1. R. Betti and O. A. Hurricane, “*Inertial-confinement fusion with lasers*,” *Nature Physics* **12**, 435 (2016).
 2. S. A. Slutz et al., “*Pulsed-power-driven cylindrical liner implosions of laser preheated fuel magnetized with an axial field*.” *Physics of Plasmas* **17**, 056303 (2010).
 3. A. B. Sefkow et al., “*Design of magnetized liner inertial fusion experiments using the Z facility*.” *Physics of Plasmas* **21**, 072711 (2014).
 4. R. S. Craxton and R. L. McCrory, “*Hydrodynamics of Thermal Self-Focusing in Laser Plasmas*” *Journal of Applied Physics* **56**, 108 (1984).

5. D. Barnak, Private communication
6. J. Davies, Private communication
7. A. Harvey-Thompson, Private communication